npj | clean water

www.nature.com/npjcleanwater

ARTICLE OPEN

Check for updates

A three-dimensional antifungal wooden cone evaporator for highly efficient solar steam generation

Meihua Xie[1], Ping Zhang[1], Yizhong Cao[1], Yutao Yan[1], Zhe Wang[1]✉ and Chunde Jin[1]✉

Interfacial solar energy evaporation is an effective measure to alleviate the current global shortage of clean water resources. However, many solar evaporators are two-dimensional (2D) structured devices developed by coating light-absorbing materials on the surface of host materials, and the efficiency of solar steam generation is limited. For this reason, the present study reports a facile and environment-friendly method to construct a conical three-dimensional (3D) wooden evaporator, which uses flexible wood as the substrate and tannic acid complex as the light-absorbing material and is formed by further convolution. Reasonable structural design and material combination enable the evaporator to show excellent mildew resistance and highly efficient evaporation performance. The black decoration considerably improves the wood light absorption, resulting in high absorbance (>90%) of DW-TA-Fe^{3+} in the wavelength range of 200–800 nm. The water evaporation rate of the wooden cone evaporator can reach up to 1.79 kg m^{-2} h^{-1}, about 1.6 times higher than that of the 2D evaporator. Moreover, the evaporator exhibits outstanding biological stability and effective desalination performance. This work is expected to offer a new direction in designing a 3D wooden evaporator for effective solar water desalination.

npj Clean Water (2023)6:12 ; https://doi.org/10.1038/s41545-023-00231-3

INTRODUCTION

Clean water scarcity is a leading pressing challenge today due to the population boom and industrial development[1–3]. To mitigate this problem, many technologies such as electrodialysis[4], membrane distillation[5], reverse osmosis[6], multi-effect distillation (MED), adsorption desalination (AD)[7–12], etc., have been used for clean water production, however, which have limited application due to the relatively complex process as well as high cost and which have limited application due to the relatively complex process as well as high cost and low standard universal performance ratio (10–13%, was calculated based on standard primary energy)[13]. Solar interfacial evaporation utilized for desalination is an effective and sustainable method to alleviate freshwater resource shortages[14–17]. Different from traditional solar evaporation (heating a large amount of water)[18–21], this technology uses a specific structure to confine energy to the light-absorbing layer, allowing for water evaporation on the structure surface, effectively reducing heat loss and achieving higher evaporation efficiency[22–27].

Various photothermal materials have been introduced into solar interfacial evaporation systems, such as nano-metal ions[28], graphene oxide[29], polypyrrole[30], etc. Efficient evaporation performance has been achieved by improving the absorption rate and reducing heat loss of photothermal evaporation devices[31–37]. By decorating metal nanoparticles into the natural wood, Zhu et al. designed a plasmonic material with a high absorption rate of 99% in the wavelength range of 200–2500 nm[38]. Feng et al. devised a solar evaporator via calcinating melamine sponges (MS). The calcinated MS with thermal insulation achieved an ultrafast solar evaporation rate (1.98 kg m^{-2} h^{-1}) and high photothermal efficiency (~92%)[39]. Yan et al. studied an ultra-light maize straw/graphene aerogel with a solar energy conversion efficiency of 95% by low-temperature hydrothermal reduction and atmospheric drying using ice crystals as templates[40]. Low-cost natural wood was used as an evaporator for solar desalination owing to its microporous structure and excellent hydrophilicity. Most research constructed planar devices by coating light-absorbing materials on the transverse and longitudinal sections of natural wood[41–44]. Plagued by complicated manufacturing and low evaporation rate, these technologies require further improvement in evaporation performance. However, the choice of materials has reached the bottleneck of efficiency, and the theoretical limit of energy conversion efficiency is hard to push further.

Recently, in order to break through the limit of theoretical efficiency, the solar evaporator was extended from original 2D to 3D structures. Compared with the 2D evaporator, the 3D version exhibited more excellent evaporation performance due to a larger evaporation area and less diffuse reflection[45–55]. For instance, Cao et al. developed an ASA 3D conical Janus evaporator with a stable evaporation rate of 1.713 kg m^{-2} h^{-1} for 14 days to 3.5% artificial seawater[56]. Wang et al. prepared an artificial photothermal cone with polypyrrole (PPy) coating and solar conversion efficiency of about 1.7 times higher than plane film[57]. Liu et al. reported a high-performance 3D photothermal catalytic spherical evaporator whose light-to-vapor efficiency exceeded the theoretical limit, reaching 217%[58]. However, the relatively complex preparation still needs further improvement.

Here, a wood-based conical evaporator was developed via wood flexibility treatment, photothermal material loading, and structural design. Delignification improved the flexibility and hydrophilicity of wood. The black tannic acid complex was used as the main material for solar photothermal harvesting. Owing to the rational structural design, multiple light reflections occurred on the device surface, and diffuse reflection was reduced, promoting light absorption. Therefore, by using this wooden cone evaporator, the evaporation rate and efficiency reached up to 1.79 kg m^{-2} h^{-1}. Furthermore, the evaporator demonstrated efficient desalination and excellent stability. Taken together, this highly efficient and highly stable wood-conical evaporation device holds great promise in solar desalination.

[1]College of Chemistry and Materials Engineering, Zhejiang A&F University, Hangzhou 311300, PR China. ✉email: wangzhe@zafu.edu.cn; jincd@zafu.edu.cn

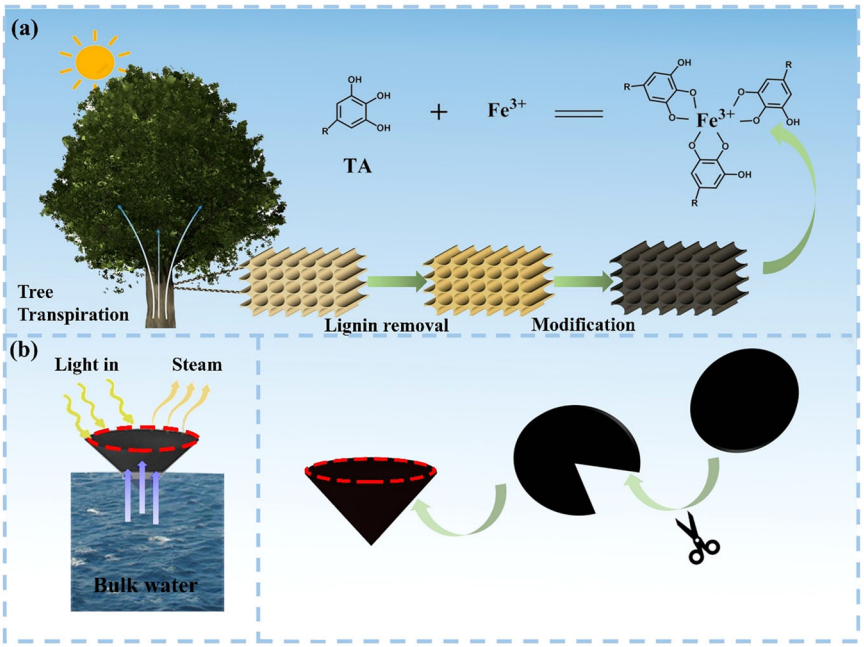

Fig. 1 Preparation of wood-conical evaporation device. a Preparation schematic diagram of photothermal conversion wood veneer. **b** 3D wood cone evaporator.

RESULT AND DISCUSSION

Inspired by natural plant transpiration, this study designs a wooden cone evaporator via successively loading tannins and iron ions on the DW surface. Different from the traditional wood evaporation device, in this work, the wood was subjected to alkaline sulfite treatment to remove partial lignin and hemicellulose, significantly improving the flexibility of the wood and overcoming the infeasibility of 3D structural shaping on the wood due to wood rigidity. In the first step, DW with improved hydrophilicity and flexibility was obtained. After a two-step immersion treatment, the light absorption layer on the wood turned from the original pale yellow to black (Fig. 1a and Supplementary Fig. 1) thanks to the complexation action between tannic acid and Fe^{3+}[59]. The 3D cone evaporator was obtained finally by further hand cutting and shaping of flexible wood with the black light absorption layer for solar seawater desalination (Fig. 1b).

Analysis of the morphology of surface morphology

The characteristic hierarchical porous structure of wood was beneficial to rapid water transportation by capillary action and excellent heat insulation[60,61]. As shown in SEM images (Fig. 2a1, a2), large amounts of channels were aligned vertically in the poplar wood and were mainly composed of wood fibers and vessels[42], which were well-preserved from poplar veneer after delignification and coating (Fig. 2b1, c1). Moreover, high-magnification images showed some spheres on the wood cell wall surface (Fig. 2c3), i.e., the tannic acid complexes on the DW-TA-Fe^{3+}. These longitudinally parallel channels were connected by the pits distributed along the vessel walls (Fig. 2c2). The 3D water transport network consisted of longitudinal channels and horizontal pits inside the wood. Furthermore, after removing partial lignin, the original densely-packed cell walls evolved into a highly loosened skeleton, and the well-aligned cellulose nanofibers in the cell wall were distinctly exposed (Supplementary Fig. 2), improving wood hydrophilicity and reducing thermal conductivity. In addition, lignin removal reduced wood stiffness and increased wood flexibility, making it feasible to construct conical devices. The intensity during folding even reached up to 180° without fracturing (Supplementary Fig. 3).

Analysis of chemical composition

The changes in chemical functional groups of wood were analyzed by FTIR spectroscopy at different treatment stages. Figure 3a shows the chemical functional groups of wood, DW, and DW-TA-Fe^{3+}, respectively. As can be seen, functional groups of lignin and hemicellulose were weakened after alkaline sulfate treatment, where the stretching vibration absorption peaks of C=O and acetoxy of hemicellulose were at 1738 and 1235 cm^{-1}[1,62], respectively, whereas the characteristic functional groups of lignin were at 1635, 1506, and 1463 cm^{-1}[1,63]. However, a characteristic peak was found at 1722 cm^{-1} in the spectrogram of the DW-TA-Fe^{3+}, which belonged to the peak of C=O in tannic acid[64,65]. The result analysis of the chemical composition also confirmed this result (Fig. 3b). The above results identified that the alkaline sulfate treatment removed part of the component, i.e., lignin and hemicellulose in the wood. Additionally, XPS patterns was used for further investigation of the chemical element composition and chemical bond situation of wood samples. As shown in Fig. 3c, the XPS survey spectrum of the DW-TA-Fe^{3+} presented three main characteristic peaks, among which C1s, O1s, and N1s were at the binding energy of 284.6, 532.2, and 399.5 eV. The Fe2p (710.6 eV) symbol was initiated from the tannic acid complex. The high-resolution C1s spectrum of the DW-TA-Fe^{3+} indicated three peaks at 284.8, 286.5, and 288.2 eV related to C-C, C-O, and C=O, respectively (Fig. 4). The spectrum of O1s revealed three peaks of C-O (532.8 eV), C=O (532.1 eV), and O-Fe (531 eV), respectively (Fig. 3d). O-Fe chemical bond was attributed to the dehydrogenation of the phenolic hydroxyl group on the tannic acid to form a chelate with Fe^{3+} (Supplementary Fig. 5). The increase in oxygen content and the presence of the O-Fe chemical bond in the DW-TA-Fe^{3+} indicated that the tannic acid complex was loaded on the wood surface (Supplementary Tab. 1). This observation was supported by the EDS mapping images of C, O and Fe elements on the DW-TA-Fe^{3+} surface (Fig. 2c6 and Supplementary Fig. 6).

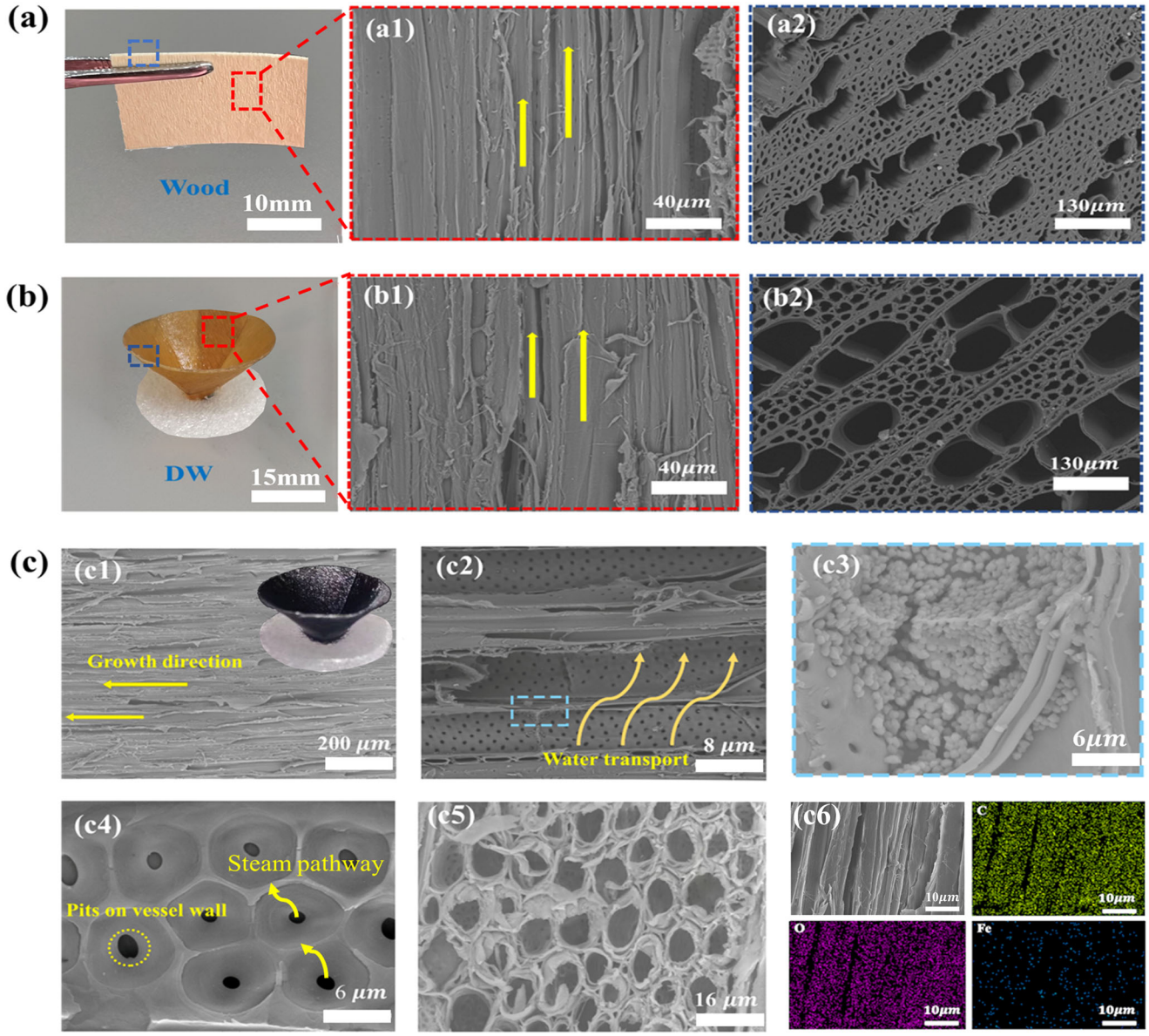

Fig. 2 The morphology and structure of wood, DW, and DW-TA-Fe^{3+}. **a**, **b** Optical images of wood and DW. **a1**, **b1** The SEM images of wood and DW in the tangential section. **a2**, **b2** The SEM images of DW and wood in cross-section. **c** The micromorphology of the DW-TA-Fe^{3+}. **c6** The EDS mapping images of the DW-TA-Fe^{3+}.

Analysis of hydrophilicity and heat behavior

Excellent hydrophilicity is the prerequisite for solar interfacial evaporation. As shown in Fig. 4a, compared with wood, DW represented greater water absorption efficiency owing to the removal of the relatively hydrophobic lignin. The water drop was fully absorbed into DW in just 3 s. DW remained hydrophilicity after TA-Fe^{3+} coating. Additionally, the assessment of the water transportation ability of the wood and DW samples using the methyl orange (MO) solution revealed the stronger capacity of DW substrate for water transport (Supplementary Fig. 7). Lignin removal not only increased the hydrophilicity but also reduced the thermal conductivity of wood[63,66]. In the dry state, the thermal conductivity of wood and DW were 0.1455 and 0.1200 W/m k, respectively (Fig. 4e). The delignification process made the wood more hydrophilic, thermally insulating, and porous, increasing the evaporation rate. The optical absorbance of wood and DW-TA-Fe^{3+} was observed using a UV-Vis-NIR spectrometer. As shown in Fig. 4b, DW-TA-Fe^{3+} displayed higher absorption capability in the wavelength range of 200–2500 nm, attributed to the coating of the black tannic acid complex and the porous structure inside the wood. Figure 4c illustrates the surface temperature change curves of the DW-TA-Fe^{3+} evaporator, DW evaporator, and water during simulated solar radiation obtained by infrared thermal imaging. After 1 h, the temperature of the 3D wooden evaporator rose to 39 °C because of the multiple light reflections on the conical cavity surface (Supplementary Fig. 8), the thermal performance of the DW-TA-Fe^{3+} evaporator is significantly higher than the other two evaporators.

Evaporation acceleration by DW-TA-Fe^{3+}

To study the photothermal conversion and evaporation of the 3D cone evaporator, a homemade water-evaporation device was used to measure water mass change during evaporation (Supplementary Fig. 9). A pearl cotton foam ring (thermal conductivity of

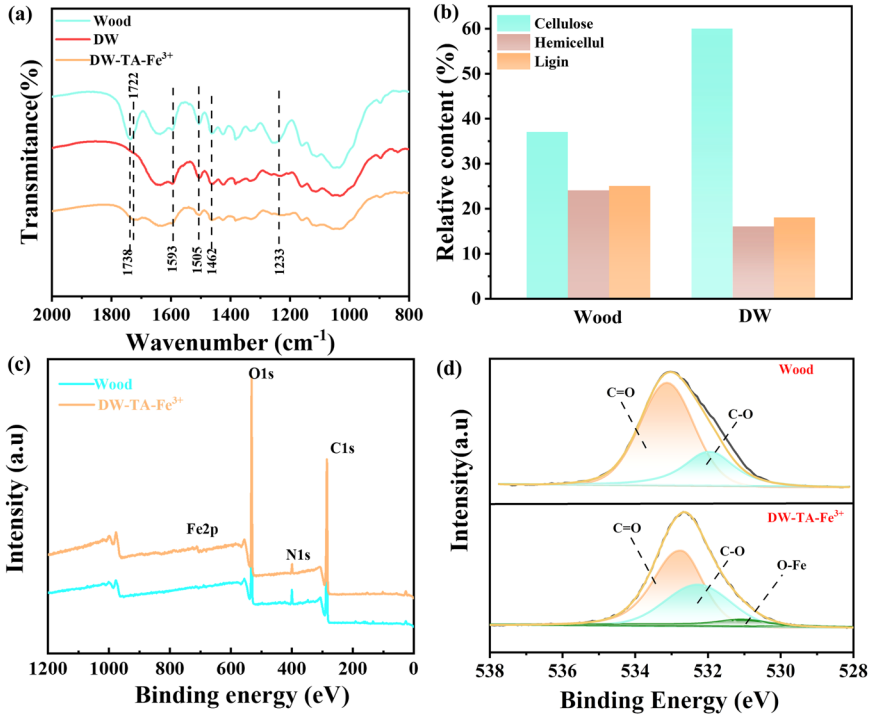

Fig. 3 The functional groups and chemical compositions of wood, DW, and DW-TA-Fe^{3+}. a The FTIR spectrum of the wood, DW and DW-TA-Fe^{3+}. **b** The relative content of cellulose, hemicellulose, and lignin in wood and DW. **c** XPS survey spectra of wood and DW-TA-Fe^{3+}. **d** High-resolution O1s peaks.

0.02965 W/m k) was used to fix the evaporator, and insulate and reduce heat loss[39,67,68]. Figure 4d showed the evaporation rate of water, 2D, and 3D evaporators (with an identical projected area). Compared with the 2D evaporator, the 3D cone evaporator significantly accelerated water evaporation under the same test conditions, and the evaporation rate was as high as 1.79 kg m^{-2} h^{-1}, about 8 and 1.6 times higher than that of water (0.22 kg m^{-2} h^{-1}) and 2D evaporators (1.11 kg m^{-2} h^{-1}), higher than many other solar steam power systems, implying an excellent evaporation performance of the 3D wooden cone evaporator.

In addition, the device-water contact area is also an important factor affecting evaporation performance. For this reason, we investigated the evaporation performance of the three systems by controlling the height at which the evaporator was immersed in water (as shown in Fig. 5a). Figure 5c shows the changes in the surface temperature of the device during solar-to-heat conversion recorded by the infrared thermal imager. After 60 min of irradiation, the temperature of the device surface (h = 5 mm) increased significantly and reached 38.8 °C. However, the temperature of the whole evaporator immersed in water was only 36 °C. As shown in Fig. 5d, the evaporation rate of devices with a minimal contact area with water reached up to 1.78 kg m^{-2} h^{-1}, while that of the whole evaporator immersed in water was just 1.18 kg m^{-2} h^{-1}. As shown in Fig. 5b, the device fully immersed in water lost much heat, and the temperature of the bulk water increased significantly. Therefore, the device-water contact area was under reasonable control, preventing energy loss from the solar absorption layer to bulk water.

Water purification performance of DW-TA-Fe^{3+}

Further, to assess the desalination performance of the 3D wooden cone evaporator, seawater obtained from the East China Sea was used for solar evaporation and purified water collection during solar evaporation. Inductively coupled plasma mass spectrometry (ICP-MS) was used to detect the ion concentration. As shown in Fig. 6a and Supplementary Table 2, the concentrations of the main ions (Na^+, Mg^{2+}, K^+, and Ca^{2+}) in the seawater after desalination were 2.01, 0.22, 0.48, and 0.04 mg L^{-1}, respectively, far less than the drinkable water standard limit defined by World Health Organization. Besides, Supplementary Fig. 10 shows the results of pH, total dissolved solids (TDS), and conductivity of seawater before and after desalination. The pH of dilute water was 6.59, conductivity was 318 us/cm, and the TDS value was 19 ppm. The test results meet the sanitary standard for drinking water (GB 5749–2006), which indicated good desalination performance of the 3D wooden cone evaporator. Figure 6b presents the stability performance of the evaporator, the evaporation rate could still reach 1.62 kg m^{-2} h^{-1} after repeated use ten times. Supplementary Fig. 11 shows the evaporation rate of DW-TA-Fe^{3+} in long-term storage of 30 days. The evaporation rate is still stable after long-term storage, clearly, the evaporation rate was also stable over the whole measured period, which undoubtedly indicated good stability and recyclability of the DW-TA-Fe^{3+} device. In order to further test the biological stability, the wood, and DW-TA-Fe^{3+} were placed in water for 15 days under natural sunlight, respectively. As shown in Fig. 6c, e, obvious mildew spots were observed on the wood surface, and the DW-TA-Fe^{3+} has no obvious mildew spots, revealing that the wood was infected by fungus in a humid state. The SEM was used to further observe the surface morphology of wood and DW-TA-Fe^{3+}. As shown in Fig. 6d, f, many mycelia were covered on the channels of the wood. Compared with those of the wood, the DW-TA-Fe^{3+} surface and interior showed no apparent mycelia aggregation, indicating a great mildew resistance. The result analysis of the DW-TA-Fe^{3+} surface after floating for 30 days under natural sunlight also confirmed this result (Supplementary Fig. 12). Alkaline sulfite treatment imparted mildew resistance to wood because partial hemicellulose (a heteropolymer of monosaccharides and the nutrients for mold) was removed from raw wood. Furthermore,

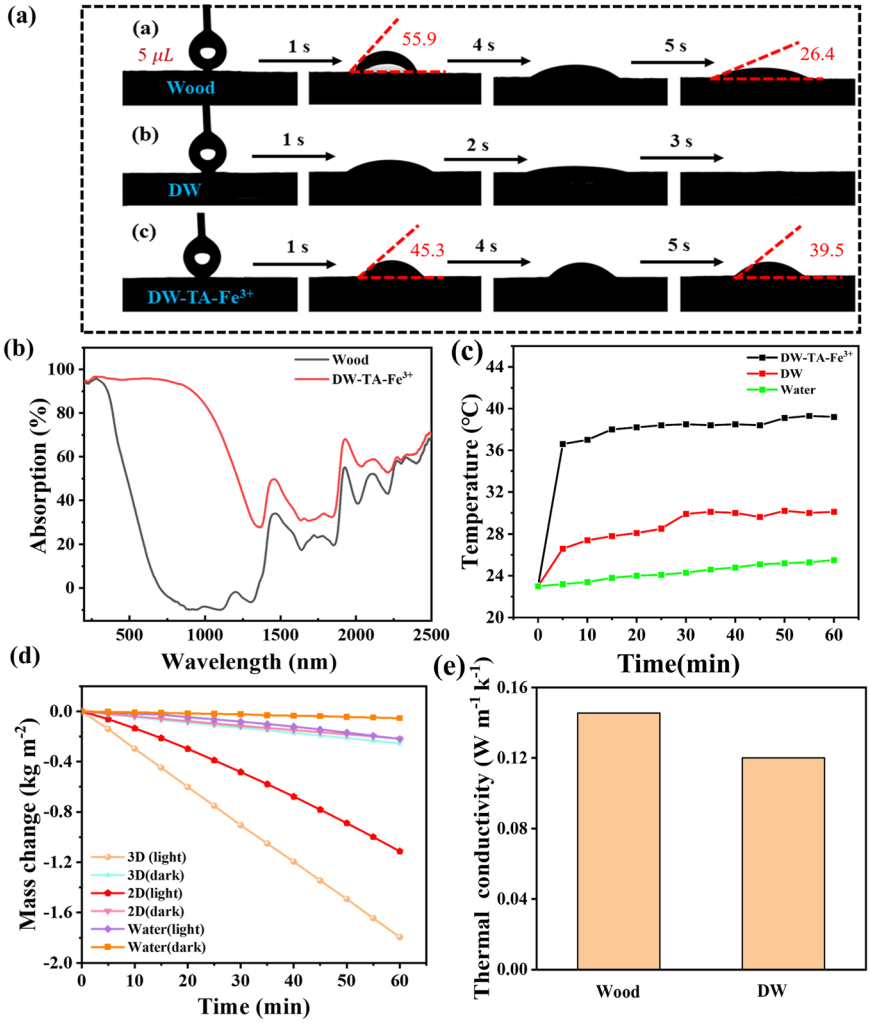

Fig. 4 The hydrophilicity, photothermal thermal, and water evaporation performance of the evaporator. a The contact angles of the wood, DW and DW-TA-Fe^{3+}. **b** The absorption of wood and DW-TA-Fe^{3+}. **c** Surface temperature curves of 3D wooden cone evaporator. **d** Water mass changes of three evaporation systems under the dark condition and one sun illumination intensity. **e** Thermal conductivities of the natural wood and DW.

the excellent antibacterial effect of tannins also plays a role in preventing mildew[69,70]. The results showed that the 3D wooden cone evaporator had satisfying stability.

Evaluation of the practical applicability of DW-TA-Fe^{3+}

The water evaporation performance of DW-TA-Fe^{3+} under natural sunlight was measured in a self-made solar distillation device. Figure 7a shows the freshwater collection process during outdoor experiments (8:00–16:00). Under natural sunlight, vapor was produced from the DW-TA-Fe^{3+} surface. Then freshwater was condensed on the inner wall of the glass dome and eventually poured from the side duct. After 8 h evaporation, ~9 mL of freshwater was collected from the side duct, and the corresponding evaporation rate reached 1.59 kg m^{-2} h^{-1} (Fig. 7b). The DW-TA-Fe^{3+} showed a weakened evaporation effect compared to that under the laboratory test condition because the natural solar illumination was lower than one solar intensity simulated by the experiment. (1 kW m^{-2}). The cost of a DW-TA-Fe^{3+} was calculated to be $ 0.12 (Supplementary Table 3). The comparison of materials component, performance, and cost between this study and other research was shown in Supplementary Table 4. The result indicated DW-TA-Fe^{3+} was an efficient and practical evaporator. Meanwhile, the daily water consumption of one adult (2–3 L) can be produced by a 1 m^2 device (3.18 kg) after 2 h under an average of about 0.66 kW m^{-2} natural sunlight.

In summary, inspired by natural plant transpiration, we developed a conical wooden photothermal evaporator of high efficiency via chemical modification and device structure design. The evaporation efficiency of the device reached 1.79 kg m^{-2} h^{-1} under one sunlight, Moreover, alkaline sulfite treatment and tannin complex loading helped to improve evaporation performance during mildew resistance, enabling the device to achieve satisfying biostability after immersion in water for up to 30 days. The DW-TA-Fe^{3+} showed the characteristics of low cost, facile preparation, and green, which provides a new idea for high-efficiency solar energy generation.

METHODS

Materials

Tannic acid (TA) and iron sulfate hydrate ($Fe_2S_3O_{12}{\cdot}xH_2O$) were provided by Macklin and used for light-absorbing material construction. Poplar veneer as a substrate was used for photothermal wood manufacturing. Sodium sulfite (Na_2SO_3) and sodium

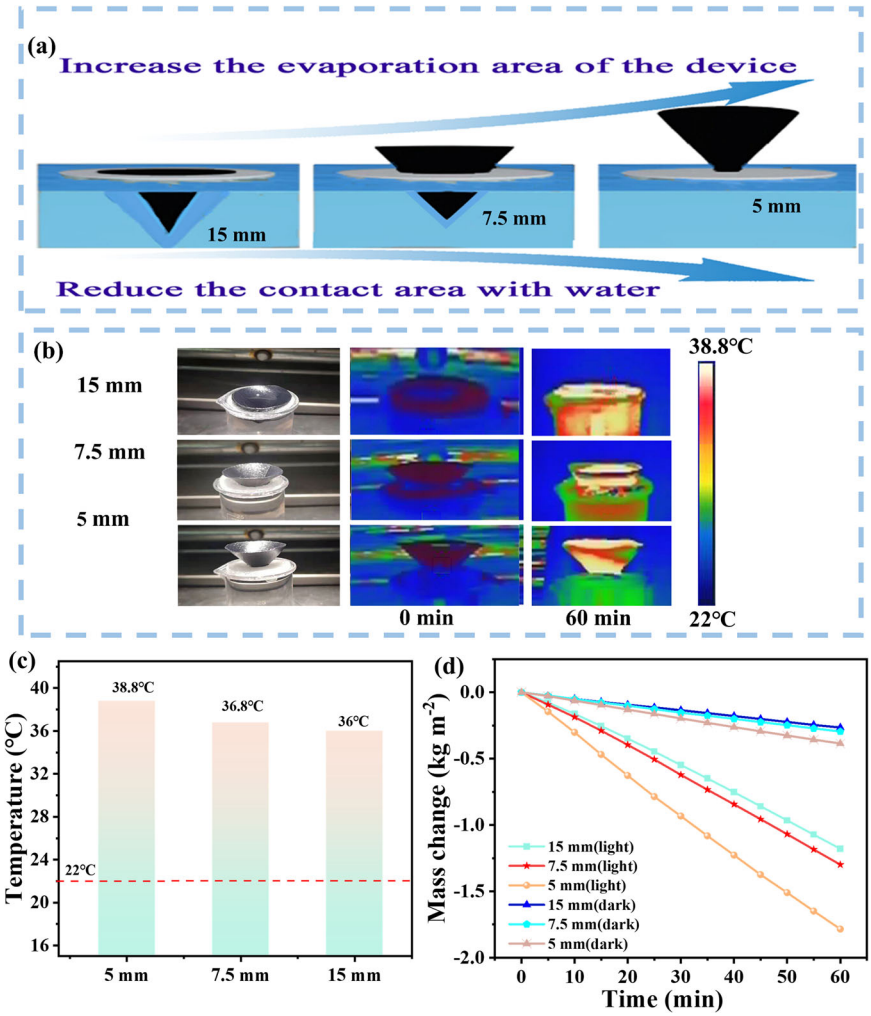

Fig. 5 Enhancement of water evaporation by reducing thermal losses. a Schematic diagram of the device at different underwater heights. **b** Surface temperature images of the three evaporation systems. **c** Surface temperature change of the three evaporation systems. **d** Water mass changes of three evaporation systems.

hydroxide (NaOH) were offered by Sinopharm Chemical and used for the lignin removal from wood. Deionized water was used throughout the experiment.

Delignification of natural wood

The wood veneers with a size of 90 mm × 90 mm × 0.55 mm (tangential × longitudinal × radial) were dipped in a mixed solution of 2.5 M NaOH and 0.4 M Na_2SO_3 (7 h, 100 °C) and then immersed in boiling water several times to remove chemicals so as to obtain the delignified wood (DW)[71].

Preparation of the 3D wooden cone evaporator

First, DW was immersed in TA aqueous solution (4% w/v) for 12 h at room temperature to prepare DW-TA. After that, the obtained DW-TA was dipped in 4% w/v $Fe_2S_3O_{12}{\cdot}xH_2O$ aqueous solution at room temperature for 2 h to realize the complexing reaction of TA and Fe^{3+} on the DW surface. Afterward, DW-TA-Fe^{3+} was cut into a circle with a diameter of 42 mm and curled up into a cone. Finally, the cone was fixed by a mold to prepare a 3D wooden cone evaporator.

Characterization

The microtopography of wood, DW, and DW-TA-Fe^{3+} was investigated by SEM (TM3030, Hitachi, Japan). The surface element distribution of DW-TA-Fe^{3+} was measured by SEM-EDS (SU8010, Hitachi, Japan) mapping system. The surface chemical functional groups, compositions, and bonded valence were analyzed using FTIR (IR-Prestige 21, Shimadzu, Japan) XPS (Thermo Scientific K-Alpha, Thermo Fisher Scientific, Germany). The wood composition was determined by paradigm washing (GB/T20805–2006 and GB/T20806–2006 standard). The sunlight absorption characteristics of the wood and DW-TA-Fe^{3+} were detected using a UV-vis-NIR (UV 3600Plus, Shimazu, Japan) at the range of 200–2500 nm. Hydrophilicity was assessed by the OCA100 contact angle system (Dataphysics, Germany). The concentration of metal ions in the collected water was appraised via ICP-MS (Agilent 720ES, Shimazu, Japan) inductively coupled plasma mass spectrometer.

Solar water evaporation performance measurement

The 3D cone evaporator was fixed by a pearl cotton foam ring with a diameter of 30 mm on the water surface in the container. The solar water evaporation performance was tested using a solar simulator (CEL-HXF300H5, China) with a standard solar spectrum (AM 1.5 G). The electronic balance (FA200, China) with an accuracy of 0.1 mg was used to record mass changes. The surface temperature of the evaporator was measured by an infrared camera (DS-2TPH10-3AUF).

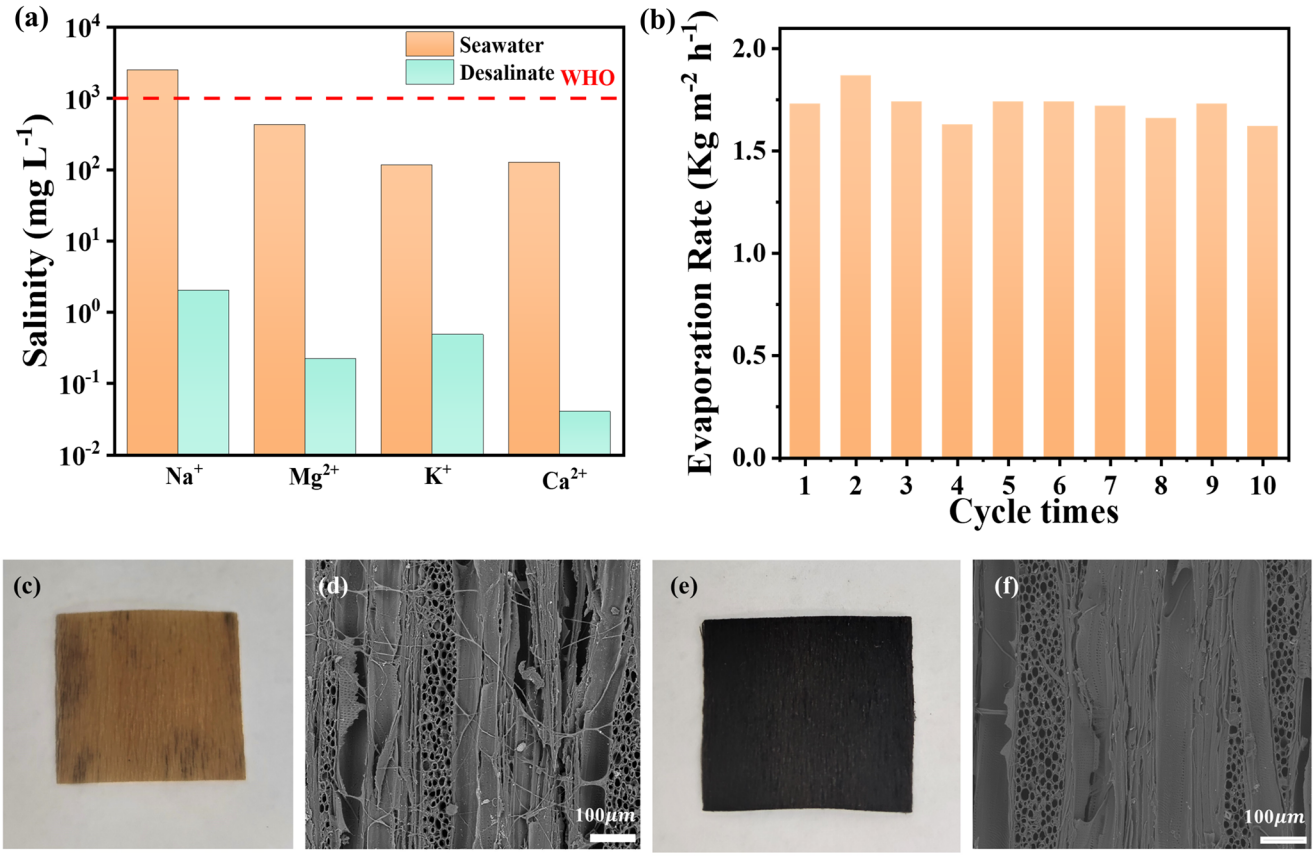

Fig. 6 The desalination and stability performance of DW-TA-Fe^{3+}. a Ion concentrations of Na^+, Mg^{2+}, K^+, and Ca^{2+} of seawater and desalted water. **b** Cycle performance of the DW-TA-Fe^{3+}. **c**, **d** The morphology of wood surface after floating 15 days under natural sunlight. **e**, **f** The morphology of DW-TA-Fe^{3+} surface after floating 15 days under natural sunlight.

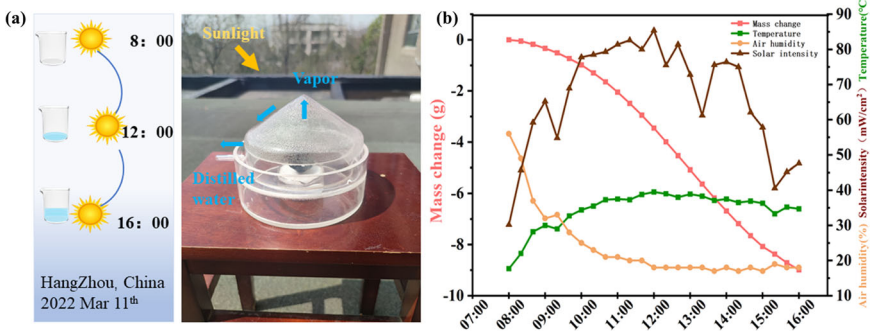

Fig. 7 Practical evaporation applications of DW-TA-Fe^{3+}. a The outdoor experiment for water evaporation. **b** 8:00 to 16:00 with varying ambient temperature, air humidity, and solar intensity.

DATA AVAILABILITY

The data that support the findings of this study are available from the corresponding author upon reasonable request.

Received: 13 September 2022; Accepted: 10 February 2023;
Published online: 20 February 2023

REFERENCES

1. Goh, P. S., Matsuura, T., Ismail, A. F. & Ng, B. C. The water-energy nexus: solutions towards energy-efficient desalination. *Energy Technol.* **5**, 1136–1155 (2017).
2. Jia, C., Yan, P., Liu, P. & Li, Z. Energy industrial water withdrawal under different energy development scenarios: a multi-regional approach and a case study of China. *Renew. Sust. Energ. Rev.* **135**, 110224 (2021).
3. Damkjaer, S. & Taylor, R. The measurement of water scarcity: defining a meaningful indicator. *Ambio* **46**, 513–531 (2017).
4. Venugopal, K. & Dharmalingam, S. Utilization of bipolar membrane electrodialysis for salt water treatment. *Water Environ. Res.* **85**, 663–670 (2013).
5. Camacho, L. et al. Advances in membrane distillation for water desalination and purification applications. *Water* **5**, 94–196 (2013).
6. Cingolani, D., Eusebi, A. L. & Battistoni, P. Osmosis process for leachate treatment in industrial platform: economic and performances evaluations to zero liquid discharge. *J. Environ. Manag.* **203**, 782–790 (2017).
7. Shahzad, M. W., Burhan, M., Ang, L. & Ng, K. C. in *Emerging Technologies for Sustainable Desalination Handbook* (ed. Gude, V. G.) Ch. 1 (Elsevier Science, 2018)
8. Feria-Díaz, J. J., López-Méndez, M. C., Rodríguez-Miranda, J. P., Sandoval-Herazo, L. C. & Correa-Mahecha, F. Commercial thermal technologies for desalination of water from renewable energies: a state of the art review. *Processes* **9**, 262 (2021).

9. Ahmad, N. A., Goh, P. S., Yogarathinam, L. T., Zulhairun, A. K. & Ismail, A. F. Current advances in membrane technologies for produced water desalination. *Desalination* **493**, 114643 (2020).
10. Errico, M. et al. Membrane assisted reactive distillation for bioethanol purification. *Chem. Eng. Process* **157**, 108110 (2020).
11. Saren, S., Mitra, S., Miyazaki, T., Ng, K. C. & Thu, K. A novel hybrid adsorption heat transformer – multi-effect distillation (AHT-MED) system for improved performance and waste heat upgrade. *Appl. Energy* **305**, 117744 (2022).
12. Son, H. S., Shahzad, M. W., Ghaffour, N. & Ng, K. C. Pilot studies on synergetic impacts of energy utilization in hybrid desalination system: multi-effect distillation and adsorption cycle (MED-AD). *Desalination* **477**, 114266 (2020).
13. Shahzad, M. W., Burhan, M. & Ng, K. C. A standard primary energy approach for comparing desalination processes. *NPJ Clean. Water* **2**, 1–7 (2019).
14. Zheng, X., Chen, D., Wang, Q. & Zhang, Z. Seawater desalination in China: retrospect and prospect. *Chem. Eng. J.* **242**, 404–413 (2014).
15. Werber, J. R., Osuji, C. O. & Elimelech, M. Materials for next-generation desalination and water purification membranes. *Nat. Rev. Mater.* **1**, 1–15 (2016).
16. Mahmoud, K. A., Mansoor, B., Mansour, A. & Khraisheh, M. Functional graphene nanosheets: the next generation membranes for water desalination. *Desalination* **356**, 208–225 (2015).
17. Homaeigohar, S. & Elbahri, M. Graphene membranes for water desalination. *NPG Asia Mater.* **9**, e427–e427 (2017).
18. Li, X. et al. Enhancement of interfacial solar vapor generation by environmental energy. *Joule* **2**, 1331–1338 (2018).
19. Brongersma, M. L., Halas, N. J. & Nordlander, P. Plasmon-induced hot carrier science and technology. *Nat. Nanotechnol.* **10**, 25–34 (2015).
20. Ni, G. et al. Volumetric solar heating of nanofluids for direct vapor generation. *Nano Energy* **17**, 290–301 (2015).
21. Wang, X., Ou, G., Wang, N. & Wu, H. Graphene-based recyclable photo-absorbers for high-efficiency seawater desalination. *ACS Appl. Mater. Interfaces* **8**, 9194–9199 (2016).
22. Ghasemi, H. et al. Solar steam generation by heat localization. *Nat. Commun.* **5**, 4449 (2014).
23. Han, X. et al. Intensifying heat using MOF-isolated graphene for solar-driven seawater desalination at 98% solar-to-thermal efficiency. *Adv. Funct. Mater.* **31**, 2008904 (2021).
24. Luo, X. et al. The energy efficiency of interfacial solar desalination. *Appl. Energy* **302**, 117581 (2021).
25. Mahian, O., Kianifar, A., Kalogirou, S. A., Pop, I. & Wongwises, S. A review of the applications of nanofluids in solar energy. *Int. J. Heat. Mass Transf.* **57**, 582–594 (2013).
26. Ni, G. et al. Steam generation under one sun enabled by a floating structure with thermal concentration. *Nat. Energy* **1**, 1–7 (2016).
27. Panchal, H., Patel, P., Patel, N. & Thakkar, H. Performance analysis of solar still with different energy-absorbing materials. *Int. J. Ambient. Energy* **38**, 224–228 (2015).
28. Li, S.-F., Liu, Z.-H., Shao, Z.-X., Xiao, H.-S. & Xia, N. Performance study on a passive solar seawater desalination system using multi-effect heat recovery. *Appl. Energy* **213**, 343–352 (2018).
29. Yin, Z. et al. Extremely black vertically aligned carbon nanotube arrays for solar steam generation. *ACS Appl. Mater. Interfaces* **9**, 28596–28603 (2017).
30. Wang, Z. et al. A wood–polypyrrole composite as a photothermal conversion device for solar evaporation enhancement. *J. Mater. Chem. A* **7**, 20706–20712 (2019).
31. Ghim, D., Jiang, Q., Cao, S., Singamaneni, S. & Jun, Y.-S. Mechanically interlocked 1T/2H phases of MoS2 nanosheets for solar thermal water purification. *Nano Energy* **53**, 949–957 (2018).
32. Ito, Y. et al. Multifunctional porous graphene for high-efficiency steam generation by heat localization. *Adv. Mater.* **27**, 4302–4307 (2015).
33. Li, T., Fang, Q., Xi, X., Chen, Y. & Liu, F. Ultra-robust carbon fibers for multi-media purification via solar-evaporation. *J. Mater. Chem. A* **7**, 586–593 (2019).
34. Liu, H. et al. Narrow bandgap semiconductor decorated wood membrane for high-efficiency solar-assisted water purification. *J. Mater. Chem. A* **6**, 18839–18846 (2018).
35. Wang, G. et al. Reusable reduced graphene oxide based double-layer system modified by polyethylenimine for solar steam generation. *Carbon* **114**, 117–124 (2017).
36. Yang, Y. et al. Two-dimensional flexible bilayer janus membrane for advanced photothermal water desalination. *ACS Energy Lett.* **3**, 1165–1171 (2018).
37. Wang, Y., Wu, X., Yang, X., Owens, G. & Xu, H. Reversing heat conduction loss: extracting energy from bulk water to enhance solar steam generation. *Nano Energy* **78**, 105269 (2020).
38. Zhu, M. et al. Plasmonic wood for high-efficiency solar steam generation. *Adv. Energy Mater.* **8**, 1701028 (2018).
39. Gong, F. et al. Scalable, eco-friendly and ultrafast solar steam generators based on one-step melamine-derived carbon sponges toward water purification. *Nano Energy* **58**, 322–330 (2019).
40. Kong, Y. et al. Self-floating maize straw/graphene aerogel synthesis based on microbubble and ice crystal templates for efficient solar-driven interfacial water evaporation. *J. Mater. Chem. A* **8**, 24734–24742 (2020).
41. Wang, M., Wang, P., Zhang, J., Li, C. & Jin, Y. A ternary Pt/Au/TiO2 -decorated plasmonic wood carbon for high-efficiency interfacial solar steam generation and photodegradation of tetracycline. *ChemSusChem* **12**, 467–472 (2019).
42. Li, T. et al. Scalable and highly efficient mesoporous wood-based solar steam generation device: localized heat, rapid water transport. *Adv. Funct. Mater.* **28**, 1707134 (2018).
43. Liu, K. K. et al. Wood-graphene oxide composite for highly efficient solar steam generation and desalination. *ACS Appl. Mater. Interfaces* **9**, 7675–7681 (2017).
44. Zou, Y. et al. Boosting solar steam generation by photothermal enhanced polydopamine/wood composites. *Polymer* **217**, 123464 (2021).
45. Li, Y. et al. 3D-printed, all-in-one evaporator for high-efficiency solar steam generation under 1 Sun illumination. *Adv. Mater.* **29**, 1700981 (2017).
46. Hong, S. et al. Nature-inspired, 3D origami solar steam generator toward near full utilization of solar energy. *ACS Appl. Mater. Interfaces* **10**, 28517–28524 (2018).
47. Zhang, L., Li, R., Tang, B. & Wang, P. Solar-thermal conversion and thermal energy storage of graphene foam-based composites. *Nanoscale* **8**, 14600–14607 (2016).
48. Tu, C. et al. A 3D-structured sustainable solar-driven steam generator using superblack nylon flocking materials. *Small* **15**, e1902070 (2019).
49. Pham, T. T. et al. Durable, scalable and affordable iron (III) based coconut husk photothermal material for highly efficient solar steam generation. *Desalination* **518**, 115280 (2021).
50. Shao, B. et al. A general method for selectively coating photothermal materials on 3D porous substrate surfaces towards cost-effective and highly efficient solar steam generation. *J. Mater. Chem. A* **8**, 24703–24709 (2020).
51. Yuan, B. et al. A low-cost 3D spherical evaporator with unique surface topology and inner structure for solar water evaporation-assisted dye wastewater treatment. *Adv. Sustain. Syst.* **5**, 2000245 (2020).
52. Xu, Y. et al. Origami system for efficient solar driven distillation in emergency water supply. *Chem. Eng. J.* **356**, 869–876 (2019).
53. Kim, K., Yu, S., Kang, S.-Y., Ryu, S.-T. & Jang, J.-H. Three-dimensional solar steam generation device with additional non-photothermal evaporation. *Desalination* **469**, 114091 (2019).
54. Shi, Y. et al. A 3D photothermal structure toward improved energy efficiency in solar steam generation. *Joule* **2**, 1171–1186 (2018).
55. Sui, Y., Hao, D., Guo, Y., Cai, Z. & Xu, B. A flowerlike sponge coated with carbon black nanoparticles for enhanced solar vapor generation. *J. Mater. Sci.* **55**, 298–308 (2019).
56. Cao, N. et al. A self-regenerating air-laid paper wrapped ASA 3D cone-shaped Janus evaporator for efficient and stable solar desalination. *Chem. Eng. J.* **397**, 125522 (2020).
57. Wang, Y. et al. Improved light-harvesting and thermal management for efficient solar-driven water evaporation using 3D photothermal cones. *J. Mater. Chem. A* **6**, 9874–9881 (2018).
58. Liu, H. et al. Conformal microfluidic-blow-spun 3D photothermal catalytic spherical evaporator for omnidirectional enhanced solar steam generation and CO_2 reduction. *Adv. Sci.* **8**, e2101232 (2021).
59. Gong, Y. et al. Towards suppressing dielectric loss of GO/PVDF nanocomposites with TA-Fe coordination complexes as an interface layer. *J. Mater. Sci. Technol.* **34**, 2415–2423 (2018).
60. Mehrkhah, R., Goharshadi, E. K. & Mohammadi, M. Highly efficient solar desalination and wastewater treatment by economical wood-based double-layer photoabsorbers. *J. Ind. Eng. Chem.* **101**, 334–347 (2021).
61. Kuang, Y. et al. A high-performance self-regenerating solar evaporator for continuous water desalination. *Adv. Mater.* **31**, e1900498 (2019).
62. Guan, H., Cheng, Z. & Wang, X. Highly compressible wood sponges with a spring-like lamellar structure as effective and reusable oil absorbents. *ACS Nano* **12**, 10365–10373 (2018).
63. Ghafurian, M. M. et al. Enhanced solar desalination by delignified wood coated with bimetallic Fe/Pd nanoparticles. *Desalination* **493**, 114657 (2020).
64. Sahiner, N., Butun Sengel, S. & Yildiz, M. A facile preparation of donut-like supramolecular tannic acid-Fe(III) composite as biomaterials with magnetic, conductive, and antioxidant properties. *J. Coord. Chem.* **70**, 3619–3632 (2017).
65. Huang, Y., Lin, Q., Yu, Y. & Yu, W. Functionalization of wood fibers based on immobilization of tannic acid and in situ complexation of Fe (II) ions. *Appl. Surf. Sci.* **510**, 145436 (2020).
66. Song, L., Zhang, X.-F., Wang, Z., Zheng, T. & Yao, J. Fe3O4/polyvinyl alcohol decorated delignified wood evaporator for continuous solar steam generation. *Desalination* **507**, 115024 (2021).

67. Li, X. et al. Graphene oxide-based efficient and scalable solar desalination under one sun with a confined 2D water path. *Proc. Natl Acad. Sci.* **113**, 13953–13958 (2016).
68. Li, X. Q. et al. Three-dimensional artificial transpiration for efficient solar waste-water treatment. *Natl Sci. Rev.* **5**, 70–77 (2018).
69. Ma, M., Dong, S., Hussain, M. & Zhou, W. Effects of addition of condensed tannin on the structure and properties of silk fibroin film. *Polym. Int.* **66**, 151–159 (2017).
70. Jiang, P. et al. Synthesis of flame-retardant, bactericidal, and color-adjusting wood fibers with metal phenolic networks. *Ind. Crops Prod.* **170**, 113796 (2021).
71. Song, J. et al. Processing bulk natural wood into a high-performance structural material. *Nature* **554**, 224–228 (2018).

ACKNOWLEDGEMENTS

This work was supported by the National Natural Science Foundation of China (32001257 and 31971739).

AUTHOR CONTRIBUTIONS

M.X. conducted the experiments and wrote the article. P.Z. assisted in the experiments, analyze, and discuss results. Y.C., Y.Y., C.J., and Z.W. proposed research topics and Writing—review and editing.

COMPETING INTERESTS

The authors declare no competing interests.

ADDITIONAL INFORMATION

Supplementary information The online version contains supplementary material available at https://doi.org/10.1038/s41545-023-00231-3.

Correspondence and requests for materials should be addressed to Zhe Wang or Chunde Jin.